Materials and Design 160 (2018) 772–782

Contents lists available at ScienceDirect

Materials and Design

journal homepage: www.elsevier.com/locate/matdes

Thermostructural observation and adaptive control of fractal structure in ball-milled materials

Matteo Aureli[a,*], Abdelaziz Saeed Mohamed Alzaabi[b], Aseel Gamal Suliman Hussien[b], Constantine C. Doumanidis[c], Syed Murtaza Jaffar[b], I.E. Gunduz[d], Claus Rebholz[e], Nikolaos Kostoglou[f], Yiliang Liao[a], Charalabos C. Doumanidis[b,g]

[a]Mechanical Engineering Department, University of Nevada, Reno 1664 N. Virginia Street, Reno, NV 89557-0312, USA
[b]Department of Mechanical Engineering, Khalifa University, Abu Dhabi, United Arab Emirates
[c]Department of Electrical and Computer Engineering, Aristotelian University of Thessaloniki, Greece
[d]School of Mechanical Engineering, Purdue University, West Lafayette, IN 47907, USA
[e]Department of Mechanical & Manufacturing Engineering, University of Cyprus, Nicosia, Cyprus
[f]Department of Physical Metallurgy and Materials Testing, Montanuniversität Leoben, Austria
[g]Office of the Provost, Nazarbayev University, Astana, Kazakhstan

HIGHLIGHTS

- Thermostructural modeling and regulation of ball milling is investigated to address challenges of unavailable measurements
- An adaptive control system for the ball milled particulate microstructure was introduced and tested in the laboratory
- The control scheme was designed based on heat transfer and fractal structure dynamics of the process
- Adaptation was achieved by comparison of the temperature predictions of the model to infrared thermal measurements
- The system achieves the desired refinement in ball milled particulate microstructure by controlling process duration

GRAPHICAL ABSTRACT

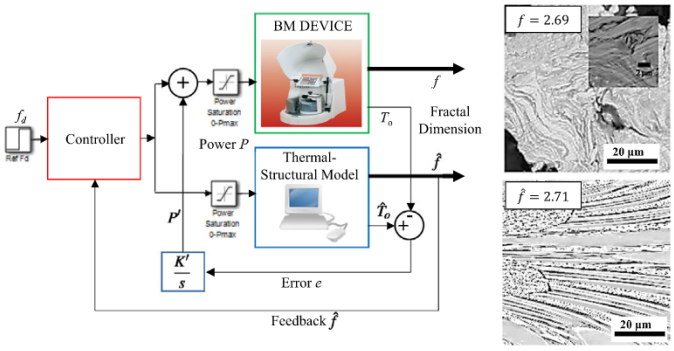

ARTICLE INFO

Article history:
Received 24 August 2018
Received in revised form 5 October 2018
Accepted 7 October 2018
Available online 10 October 2018

ABSTRACT

This research introduces dynamic modeling and real-time control of fractal structure in particulate materials fabricated by the ball milling process, specifically addressing challenges of unavailable real-time non-destructive and non-invasive imaging measurements in the enclosed rotating vials. A description of the internal temperature dynamics in the container is established along with a thermal regulator based on external temperature feedback. The fractal dimension is introduced as a structural measure, and its dynamics is established via an analytical formulation through a lumped model, along with a full thermostructural computational model of the ball milling particulate microstructure. These models are used as real-time observers of inaccessible internal states during the process. In addition, they are used as model references

* Corresponding author.
E-mail address: maureli@unr.edu (M. Aureli).

https://doi.org/10.1016/j.matdes.2018.10.010

Keywords:
Ball milling
Adaptive control
Aluminum alloys
Fractal dimension

in an adaptive control system, regulating the fractal structure with adaptation via external temperature measurements, available experimentally via an infrared thermocouple. The controller is designed on the basis of the dynamic models and is tested experimentally. The controller is demonstrated to command the duration of the process at steady conditions to obtain the necessary thermal exposure yielding the desired microstructure for the ball-milled particulates.

1. Introduction

Reactive multilayers, such as Ni-Al nanostructured foils deposited by physical vapor deposition (PVD) [1], are of contemporary interest in research and practice for rapid thermal processing and soldering in microelectronics, self-heated welding and self-curing materials in construction, local hyperthermia and cauterization in biomedicine, and other applications [2]. Upon their ignition, self-propagating exothermic reaction (SPER) and high-temperature synthesis of intermetallic compounds result in high enthalpic release and adiabatic temperatures. The thermal performance of such materials has been studied experimentally and numerically [3], and was found to depend critically on the reactive material nanostructure, such as the bilayer thickness (Fig. 1a). Clearly, finer nanolayers yield a higher specific interfacial surface in the material, therefore promoting interlayer heat conduction and metal diffusion across the foil. These, in turn, lower the required ignition temperature and enhance the propagation velocity of the reaction front along the multilayers [3].

An attractive alternative fabrication route to magnetron sputtering is offered by ball milling (BM) of metallic powders [4] into reactive globular agglomerates with internal lamellar networks (Fig. 1b). Unlike the deterministically nanostructured PVD multilayers, the stochastic nature of BM collisions results into particulates with random, self-similar structures across multiple dimensional scales [5]. Rather than a single bilayer spacing, such fractal architectures are described by their fractal dimension [6,7] (or Hausdorff dimension), ranging from a value of 2 for planar simple interfaces (Fig. 1a), towards 3 for space-filing complex boundaries (Fig. 1b). Upon heating the BM particulates, finer-scaled regions ignite first at lower temperatures, thus reacting and releasing heat. This raises the temperature of adjacent coarser areas to ignition, which in turn propagates the SPER in a cascading fashion. Conversely, large monometallic domains tend to diffuse the heat from their interface towards the bulk, thus lowering the temperature and quenching further heat and mass transport, often arresting the SPER front. Thus, it is important to control the particulates microstructure, as produced by BM, to guarantee their desired reactivity.

The relationship of the particulate structure on BM process conditions has been studied experimentally, see Ref. [8] and references therein, and recently also through a real-time, predictive computational model [9]. This direct process-structure connection offers prediction insights to ball milling (Fig. 1c) and enables off-line material design and optimization. The inverse relation of microstructure control via real-time modulation of the process conditions is also of particular practical importance. However, closed-loop control based on feedback measurements of salient in-process variables is impeded by real-time inaccessibility of ball milling, which occurs within hermetically closed rotating vials, usually in planetary motion. In addition, the violent mechanical impact conditions existing inside the BM vials are destructive for potential sensor probes or other intrusive measurement systems. Therefore, BM control efforts in the literature have been limited at the industrial system level, using empirical models (mostly for grinding) and resorting to interrupted process sampling for off-line quality monitoring and statistical process control [10,11].

In contrast to such approaches, and complementary to them, this paper addresses the core issue of in-process control of the fabricated particulate microstructure through BM. Since the product structure cannot be imaged non-invasively during uninterrupted BM, the predictions of the dynamic structural model [9] used as a real-time observer of the fractal dimension are employed as output for feedback. To enforce convergence between process and model, temperature estimates produced by the model are compared in real time with external non-contact temperature measurements on the BM vials, and the error is used to drive an adaptive control scheme.

The rest of the paper is organized as follows. Section 2 establishes a thermal description for temperature regulation of the BM device. Section 3 quantifies the influence of thermal exposure to the particulate structure via the introduction of the fractal dimension. A controller for the fractal dimension is designed and validated computationally via the full thermostructural model. Section 4 introduces an adaptation scheme based on the output of real-time model execution, employed as an observer, and model reference. The proposed control scheme is tested experimentally on a laboratory BM setting with infrared thermometry. Conclusions and further issues arising from this research are summarized in Section 5.

2. Thermal description and regulation

2.1. Linearized model of BM heat transfer

A schematic planetary ball milling setup is shown in Fig. 2, along with a cut-off section of a single vial with relevant nomenclature. The electrical power P is converted to mechanical power P_m into the rotating vials. The mechanical power is, in turn, stored as kinetic energy E_k in the moving components and residual elastic energy E_r in the deforming vial contents, while the balance is converted into thermal power H, see Ref. [12]:

$$P = VI,\ P_m = M\omega,$$
$$\eta P = P_m = \dot{E}_k + \dot{E}_r + H \tag{1}$$

where V and I are electrical voltage and current to the device motors; M and ω the torques and angular velocities at the containers; and η is the useful thermal efficiency of the device, accounting for electrical motor, aerodynamic and friction losses in its transmission, to be later calibrated experimentally. The electrical and mechanical transients of the BM process, with typical characteristic times of the order of seconds during acceleration and deceleration of the device, are ignored in the thermal modeling, which exhibits temperature transients of several minutes, as schematically represented in Fig. 3. Inner-loop control of the rotation servosystems quickly achieves electromechanical steady state (i.e. $\dot{E}_k = 0$, $\dot{E}_r = 0$), so that it can be safely assumed that $H = \eta P$ during the dominant thermal dynamics of BM. As detailed later, it is further assumed that all heat H is generated via inelastic effects, i.e. plastic yield and friction slip in the BM materials, while enthalpy released via interface diffusion and premature reaction in the particulates during BM is ignored.

The dynamics of heat transfer is formulated for a single ideal cylindrical vial with flat lid, made of homogeneous and isotropic

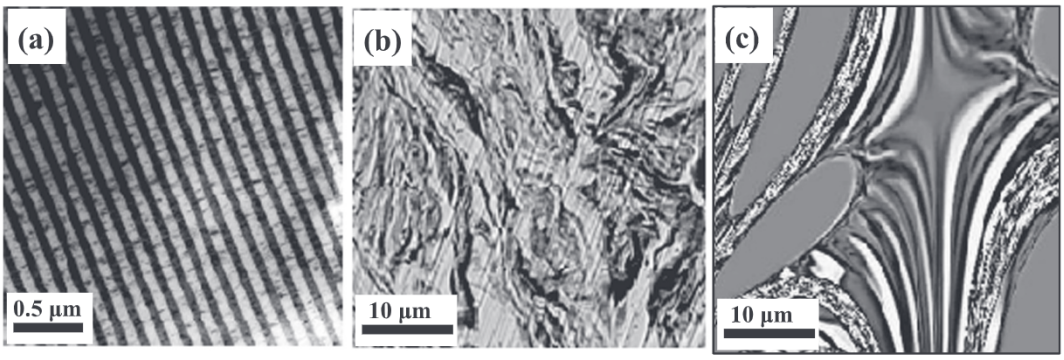

Fig. 1. Reactive Ni-Al multilayer micrographs (bright phase: Ni; dark phase: Al). (a): PVD sputtered nanolayer foil, (b): Ball-milled particulate. (c): Simulated BM structure.

conductive material (e.g. stainless steel), and dimensioned as in Fig. 2. The thermal characteristics of the container are [13]:

$$r_m = \frac{r_o - r_i}{\ln(r_o/r_i)}, \quad R_v = \frac{r_o - r_i}{k2\pi r_m(l+d)}, \quad R_l = \frac{d}{k\pi r_m^2},$$
$$R = \left(\frac{1}{R_v} + \frac{2}{R_l}\right)^{-1}, \quad C = \rho_{SS}c_{SS}[\pi r_o^2(l+2d) - \pi r_i^2 l] \tag{2}$$

where k is the thermal conductivity, ρ_{SS} is the density and c_{SS} is the specific heat capacity of the container material; r_m is the effective cylindrical radius, R_v and R_l are the conduction resistances of the vial cylindrical wall and lid or bottom, respectively. In Eq. (2), R is the composite conductive resistance, as the vial surfaces transfer heat in parallel, and C is the thermal capacity of the container. Conductive heat losses of the vial bottom to external support elements on the BM turntable and lid fixtures are neglected.

Inside the BM vial, the particulate materials, milling balls, and vial surfaces are assumed in macroscopic thermal equilibrium at an average temperature T_i, because of their efficient mixing and heat transfer, via conduction at the collision surfaces and radiation in the fully enclosed cavity [14]. Conduction across minor temperature differences inside the vial is neglected by the model. By neglecting formation of intermetallics due to inadvertent reaction during the fabrication, the thermal capacity of the vial contents C' is determined via the law of mixtures [13]:

$$C' = N_b\left(\rho_{SS}\frac{4}{3}\pi r_b^3\right)c_{SS} + m_{Ni}c_{Ni} + m_{Al}c_{Al} \tag{3}$$

where N_b is the number and r_b the radius of milling balls, and m_i, c_i the masses and specific heat capacities of the BM metal powder loads, where subscript i takes on the value Ni and Al for nickel and aluminum, respectively.

Outside the BM vial, heat loss is assumed to be due to forced convection from the rotating containers to the ambient gas at room temperature T_a, and to radiation from an average surface temperature T_o of the container walls, assumed uniform because of their efficient conduction. Due to the relatively low external temperature $T_o(\sim 100°C)$, the composite surface heat loss can be linearized to an equivalent convection term. Specifically, by denoting with $A_v = 2\pi r_o(l+2d)$ and $A_l = \pi r_o^2$ the surface areas for the vial and lid or bottom surfaces, and with $A = A_v + 2A_l$ the total external surface area, the effective convection coefficient h can be determined from [13]

$$[h_vA_v + 2h_lA_l](T_o - T_a) + \epsilon\varsigma A\left(T_o^4 - T_a^4\right) = hA(T_o - T_a) \tag{4}$$

so that $h = [h_vA_v + 2h_lA_l]/A + \epsilon\varsigma(T_o + T_a)\left(T_o^2 + T_a^2\right)$, where h_v, h_l are the convection coefficients for the vial and lid or bottom surfaces, ϵ the surface emissivity and ς the Stefan-Boltzmann radiation constant. With this definition, $R' = 1/(hA)$ is the composite convective resistance of the container, transferring heat in series to its conductive walls. The convection coefficients h_v, h_l for the complex gas flow field around the containers in planetary motion need to be determined numerically. Also, the temperature dependence of the effective convection coefficient h further complicate its evaluation. To obviate this difficulty, an effective value of h will be calibrated experimentally in the following.

2.2. BM thermal dynamics

According to the previous analysis, the energy balance equations can be derived from Eqs. (1)–(4) and written as follows, see Ref. [13]:

$$H = C'\frac{dT_i}{dt} + \frac{T_i - T_o}{R}$$
$$\frac{T_i - T_o}{R} = C\frac{d}{dt}\left(\frac{T_i - T_o}{2}\right) + \frac{T_o - T_a}{R'}. \tag{5}$$

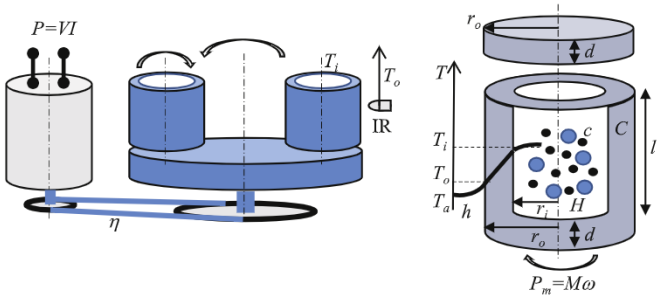

Fig. 2. Schematic arrangement of planetary ball mill (left) and BM vial for thermal analysis (right).

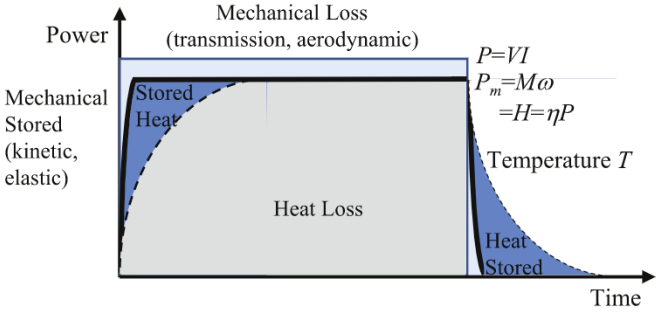

Fig. 3. Power response over time and energy transfer during BM run duration.

By solving the system of two ordinary differential equations (ODE's) using Laplace transforms (using s to denote the complex variable and a superimposed tilde to denote transformed quantities), the following transfer functions are obtained for the temperatures $\tilde{T}_i$ and $\tilde{T}_o$, with respect to thermal power $\tilde{H}$, see Ref. [15] :

$$\frac{\tilde{T}_i(s)}{\tilde{H}(s)} = G_i(s) = \frac{\frac{R}{2}\left(\frac{R}{2}+R'\right)Cs + (R+R')}{R2\,(R2+R')\,CC's^2 + [(R2+R')\,C + (R+R')C']\,s + 1}$$
$$\frac{\tilde{T}_o(s)}{\tilde{H}(s)} = G_o(s) = \frac{R'}{R2\,(R2+R')\,CC's^2 + [(R2+R')\,C + (R+R')C']\,s + 1}. \quad (6)$$

To illustrate the thermal dynamics described by Eq. (6), Fig. 4 shows of an analogous equivalent electric circuit. The linearized thermal system exhibits second order behavior because of its two energy storage elements, i.e. the container and its contents (C, C'), with a zero for $\tilde{T}_i$. For light charge of the vial (i.e. $C' \ll C$), Eq. (6) simplify to transfer functions of a first order system with dominant container dynamics. The simplified system has time constant $\tau = (R/2 + R')C$ and steady-state gains $R + R'$ for $\tilde{T}_i$ and R' for $\tilde{T}_o$:

$$\frac{\tilde{T}_i(s)}{\tilde{H}(s)} \approx \frac{\frac{R}{2}\left(\frac{R}{2}+R'\right)Cs + (R+R')}{\left(\frac{R}{2}+R'\right)Cs + 1}$$
$$\frac{\tilde{T}_o(s)}{\tilde{H}(s)} \approx \frac{R'}{\left(\frac{R}{2}+R'\right)Cs + 1}. \quad (7)$$

Fig. 5 illustrates the time responses of temperatures T_i and T_o, as solid and dashed lines, respectively, during unloaded (no powders) BM for four representative cases. Specifically, these cases report 100 or 50 milling balls of diameter 12.7 mm in vials of internal diameter 100 mm or 75 mm, respectively, operated at rotation speeds 280 rpm or 200 rpm, for which calorimetric data are available for T_i [16,17]. Calorimetric data are reported in Fig. 5 as black markers. The parameters of the thermal description in Eq. (6) have been evaluated as R = 0.014–0.020K/W, R' = 0.313–0.449K/W, C = 1875–1305J/K and C' = 435–218J/K, respectively. Good agreement is observed between the simulated responses of T_i and the experimental data. The responses of T_o are somewhat attenuated, due to the gain ratio $g = (R + R')/R'$, and slower, due to the lack of a zero in Eqs. (6) and (7).

The previous model of thermal dynamics can be employed to study the dependencies of heat transfer parameters on BM conditions. For example, the effective convection coefficient h depends on the internal vial temperature T_i through the external vial temperature T_o. By combining the transfer functions of Eqs. (6) or (7),

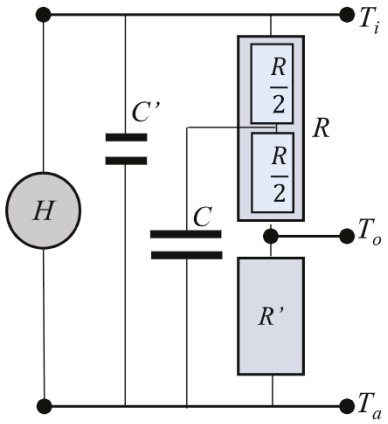

Fig. 4. Analogous circuit illustrating equivalent BM thermal dynamics.

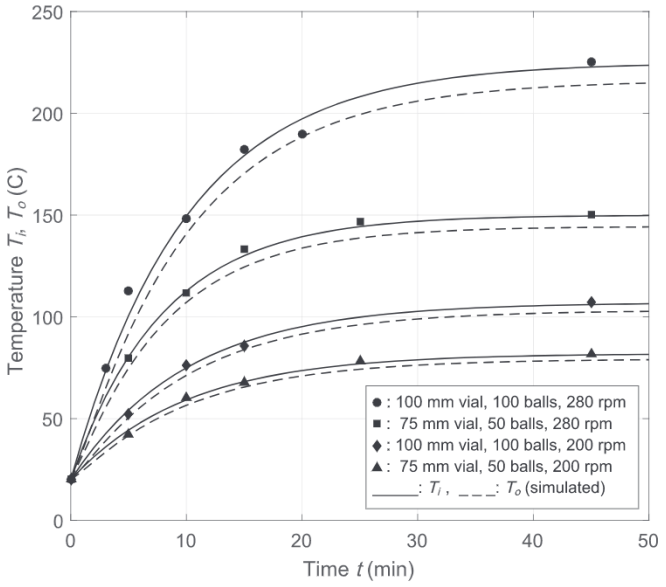

Fig. 5. Transient responses during unloaded BM of experimental measurements (markers) and simulations of internal temperature T_i (solid lines) and external temperature T_o (dashed lines).

$$\frac{\tilde{T}_o(s)}{\tilde{T}_i(s)} = \frac{R'}{\frac{R}{2}\left(\frac{R}{2}+R'\right)Cs + (R+R')} \Rightarrow$$
$$\frac{R}{2}\left(\frac{R}{2}+R'\right)C\dot{T}_o + (R+R')T_o = R'T_i. \quad (8a)$$

Eq. (4), combined with the dynamics of the external temperature T_o from Eq. (8a), defines the nonlinear dependence of coefficient h on the internal temperature T_i. At thermal steady state (i.e., $s = 0$), h can be derived from T_i in closed form using Eq. (4) as

$$\frac{T_o}{T_i} = \frac{R'}{R+R'} = \frac{1}{hAR+1} = \frac{1}{g} \Rightarrow$$
$$h = \frac{g-1}{AR} = \frac{[h_v A_v + 2h_l A_l]}{A} + \epsilon\varsigma(T_i/g + T_a)[(T_i/g)^2 + T_a^2] \quad (8b)$$

where the temperature gain ratio $g = (R + R')/R'$ can be determined experimentally as described below.

Table 1 shows the dependence of the steady-state effective convection coefficient h, as derived experimentally (i.e., calculated via $h = H/A(T_o - T_a)$, as per Eq. (4)) and determined via Eq. (8b), on the internal vial temperature T_i. The nonlinear variation $h(T_i)$ is significant within the temperature range T_i = 80–150°C of interest to BM of bimetallic powders, in which the model parameter error stays within ±8%. The model tends to overestimate the coefficient h at higher temperatures, perhaps because of unaccounted changes in radiation surface emissivity ϵ. Such temperatures, however, are not applicable to BM of reactive bimetallic systems of interest such as Ni-Al, as they approach the threshold of potentially catastrophic ignition in the vial during the fabrication process.

2.3. BM thermal control

To maintain temperature-dependent properties (such as yield stress σ_y) of the vial contents at desired values, closed-loop control of T_i may be desirable. However, since T_i is inaccessible to real-time measurements, in this work, the external temperature T_o is used

Table 1
Experimental and model-calculated variation of effective convection coefficient h on internal vial temperature T_i with only balls in the vial.

Temperature T_i (°C)	h (W/m^{2}K) Experimental value	h (W/m^{2}K) Model estimate	Error (%)
81.3	25.19	27.16	+7.81
108.1	36.14	33.25	−7.99
150.2	39.84	42.51	+6.70
212.0	57.15	64.34	+12.58

instead for in-process feedback. Specifically, the external temperature can be measured by infrared pyrometry, and T_i can be recovered through the constant steady-state gain ratio $g = T_i/T_o$.

Based on this strategy, Fig. 6 shows a simulated temperature control scheme to regulate T_i (governed by the transfer function $G_i(s)$ in Eq. (6)) to a steady reference $T_d = 200$°C, via feedback of T_o (governed by the transfer function $G_o(s)$ in Eq. (6)) for the case of 75 mm diameter vial with 50 balls described above [16]. A linear proportional-integral (PI) discrete-time controller with sampling period $t_s = 1$ min is designed for the thermal power H as [15]:

$$G_c(z) = \frac{\tilde{H}(z)}{\tilde{E}(z)} = K_T \frac{(\tau + t_s)z - \tau}{z - 1}. \tag{9a}$$

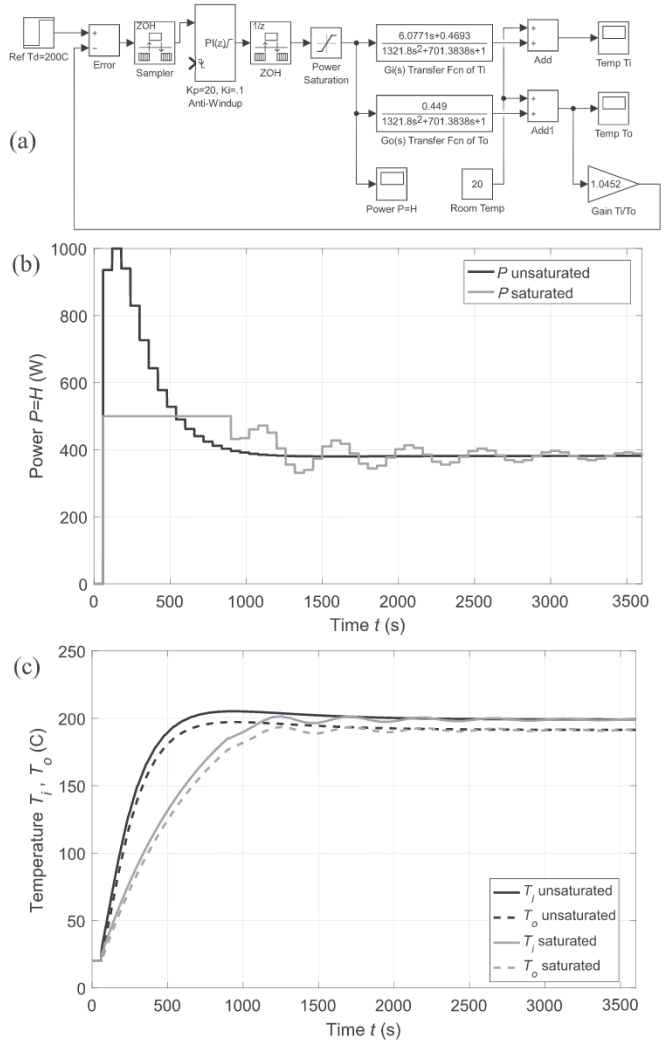

Fig. 6. Thermal regulation of the internal temperature T_i through feedback of external temperature T_o. (a): Implementation. (b): Simulated unsaturated and saturated power $P = H$. (c): Temperature responses of unsaturated and saturated T_i and T_o.

Here and in the following, discrete-time variables are indicated with superscript *, and Z-transformed quantities, in the variable z, have a superimposed tilde. In Eq. (9a), the error $\tilde{E} = \tilde{T}_d - \tilde{T}_i = \tilde{T}_d - g\tilde{T}_o$, where $g = 1.045$ and $K_T = 3.83$ is a control gain. This control law is modified to incorporate anti-windup for saturation of power $P = H$ (thermal efficiency assumed $\eta = 1$) at $P_{\max}$, according to [15]

$$H^*(j) = P^*(j) = \min[P_{\max}, H^*(j-1) + K_T\{(\tau + t_s)E^*(j) - \tau E^*(j-1)\}] \tag{9b}$$

where j is the sample index. The implementation is shown in Fig. 6a.

As an example, Fig. 6b shows the simulated time responses of power $H = P$ for unsaturated (black line, $P_{\max} = 1000$ W) and saturated (gray line, $P_{\max} = 500$ W) closed-loop control, while Fig. 6c shows the respective responses of temperatures T_i (solid lines) and T_o (dashed lines). It appears that the proposed feedback control scheme is effective in regulating the temperature T_i to T_d within a short time (approximately 10 min) for the unsaturated case. On the other hand, power saturation of the BM device prolongs this time to approximately 20 min and causes oscillatory behavior.

3. Structural formulation and control

3.1. BM structural description: lumped model

As illustrated in Fig. 3, after a short electromechanical transient, thermal power $H = \eta P$ is dissipated because of (i) plastic deformation of the milled materials and (ii) friction with the ball and vial (impactor) walls. To capture these phenomena, the powder materials are modeled as homogeneous, isotropic and non-strain hardening. They are assumed to yield plastically at equivalent von Mises stresses σ_y (dependent on temperature T_i, [18,19]), at elastic strains ε_y. These strains are small compared to the total strains ε eventually developed in BM particulates of volumes v_i. In addition, because of the assumed dry (Coulomb) friction among particulate powder boundaries and impactor walls, surface shear stresses are modeled as $q_s = \mu p$, where p is normal pressure and μ an equivalent friction coefficient. Such shear stresses initiate interfacial slip at a displacement level equal to δ_s, which is also assumed to be small with respect to total shear displacements δ of the contact areas s_i. For both heat dissipation phenomena, Fig. 7 illustrates that, after a negligible elastic/adhesion initial deformation, plastic yield and friction slip dissipate specific heat (corresponding to area OABD = ABHI), expressed as [20]:

$$H = \frac{\omega}{2\pi}\sum_i \left\{ \iiint_{v_i} \sigma_y(\varepsilon - \varepsilon_y)\mathrm{d}v + \iint_{s_i} \mu p(\delta - \delta_s)\mathrm{d}s \right\} = v\Sigma D\frac{\omega}{2\pi} = K\dot{D} \tag{10}$$

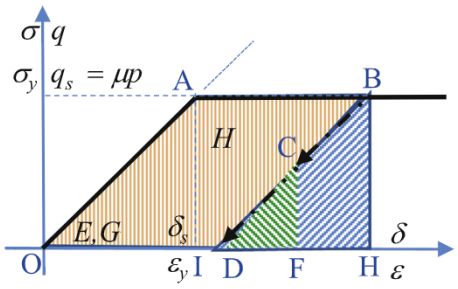

Fig. 7. Constitutive behavior of stress with strain or displacement illustrating bulk plastic yield and surface friction slip with heat dissipation in BM materials.

where v is the total volume of the vial contents, Σ an effective critical stress averaged over the volumes and interfaces of the BM powders and impactors, and $K = \Sigma v$ a thermostructural BM gain, also dependent on T_i. In Eq. (10), D can be interpreted as an equivalent average linear strain or fraction of the particulate microstructure resulting per revolution.

The parameter D can be used as a descriptor of the structural deformation of the BM particulates. Specifically, Fig. 8 shows a representative ellipsoidal particulate domain, deformed plastically from spheroidal powder. Eventually, such deformation can progress to planarized lamellar form, under the compressive BM collisions (depicted at the top). For such ellipsoidal domain, the characteristic thickness L decreases as $dD = -dL/L$. Similarly, in Fig. 8, when interfacial friction and heat release results in microwelding and joining of particles (depicted on the right boundary), the assembled total particulate exhibits a fractional internal structure at a relative depth of $dD = -dL/L$. For both plastic yield and frictional slip in Fig. 8, see [20]:

$$\dot{D} = -\frac{\dot{L}}{L} \Rightarrow D = \ln\left(\frac{L_o}{L}\right) \Rightarrow L = L_o \exp(-D). \tag{11}$$

The fractional refinement of linear (1D) dimensions in a 2D structural micrograph (as in the schematics of Fig. 8) can be associated with the change in fractal dimension f of the 3D BM particulate. In this case, the fractal dimension f, ranging between 2 and 3 for spatial interfaces, can be expressed as [6]:

$$f = \frac{L_o - L}{L_o} + 2 = 3 - \exp(-D) \Rightarrow \dot{f} = \exp(-D)\dot{D} = (3-f)\frac{H}{K} = (3-f)\frac{\eta P}{K}. \tag{12}$$

Eq. (12) describes the nonlinear dynamics of fractal structure output f with respect to BM process input P.

Note that the 3D fractal dimension f of the microstructure can be evaluated by box counting algorithms on the boundaries of a 2D section [12,20] as in Fig. 8, see Ref. [6]:

$$f = \lim_{s/S \to 0} \frac{\ln(N/n)}{\ln(S/s)} + 1 \tag{13}$$

where n, N and s, S are the numbers and sizes of quadtree boxes straddled by the interface pattern.

Fig. 9 illustrates the time responses of the fractal dimension f as predicted by the lumped model proposed in this Section (lines) in Eq. (12) for properly calibrated values of H/K, dependent on T_i. Simulation data are compared to experimental values (markers) of f, estimated from Eq. (13), obtained on experimental micrographs of BM particulate sections [9,12,14,20]. In general, very good agreement can be observed between the simulated estimates of the lumped model and the laboratory data. In Fig. 9, some experimental outliers for long BM times are attributable to boundary diffusion and premature reaction during BM fabrication. This yields continuous intermetallic phases (nickel aluminides) which smear domain boundaries and reduce the fractal dimension of the microstructure.

3.2. BM full thermostructural model

In addition to the lumped model of fractal dimension in Eq. (12), a full predictive thermostructural model of the BM particulate microstructure [9] is used for structural control. Important characteristics of the model are summarized below.

The computational model tracks the structure of a representative particulate in the BM vial on a 2D section consisting of deformed and joined monometallic domains from the original powders. These domains are modeled as warped ellipsoids [9,21], see Fig. 1c. In the model, the representative particulate and its adjoining particles and clusters are collided randomly by the BM impactors, following a Brownian-like kinematic probability density function of energies [12]. The impacted domains develop Hertzian elastic stress and strain fields, whose energy is used to determine equivalent plastic yield and friction slip displacements. As discussed in the previous subsection, these result in: (i) dissipation of internal heat H, (ii) domain deformations, determined by Castigliano's theorem methods, and (iii) interface microweld joining, via Coulomb friction [20,22]. In addition, thermal impacts generate transient local temperature increments over internal temperatures, which are estimated using Green's function techniques [14].

The evolving 2D microstructure of the particulate is thus dynamically characterized by its fractal dimension f, estimated from Eq. (13). The fractal dimension f is therefore available as a "proxy" of the actual BM structure, that cannot be imaged non-invasively during fabrication. Therefore, this computationally efficient model can be used as a real-time thermomechanical observer, running in parallel to the BM process. Specifically, for a prescribed heat input H, the

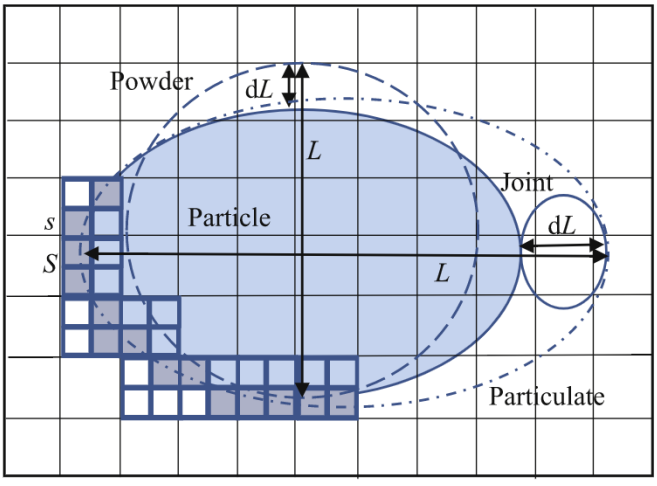

Fig. 8. Structural linear refinement $dD = -dL/L$ by plastic deformation (top) and frictional joining (right). The fractal dimension f can be evaluated via the box counting algorithm (exemplified at the lower left) of ellipsoidal BM particulates.

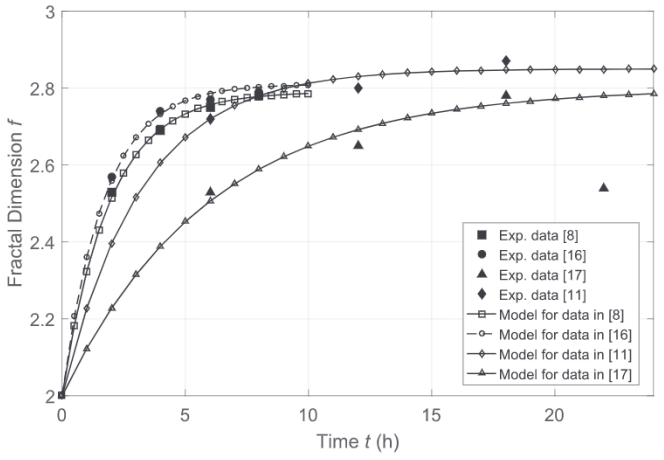

Fig. 9. Transient responses of experimental measurements of (markers) and simulated (lines) fractal dimension f during BM. Simulated fractal dimensions are obtained with the lumped model in Eq. (12).

model provides predictions of temperature and fractal dimension, to be used for feedback control in lieu of unavailable measurements.

The computational thermostructural BM model can be used to analyze the variation of lumped parameters during the process. For example, computational estimation of BM gain K can be performed via the thermostructural model on the basis of Eq. (10), from an equivalent strain D averaged over the warped ellipsoid component strains D_i in the vial per revolution

$$K(T_i) = \frac{2\pi}{\omega D} H(T_i), \quad D = \frac{\sum_i D_i v_i}{\sum_i v_i}. \tag{14}$$

Experimentally, the BM thermostructural BM gain can be determined from the variation of fractal dimension Δf on the resulting micrographs over processing time Δt. From Eq. (12),

$$K(T_i) = \frac{\Delta t}{\Delta f}(3-f)\eta P(T_i), \quad \eta = 1. \tag{15}$$

Table 2 shows time-averaged values of thermostructural BM gain K during ball milling at the internal temperature range T_i obtained in processing of Ni-Al powders [9,12,14,20], as measured experimentally via Eq. (15) and estimated computationally via Eq. (14).

The estimation error of the BM gain K remains within ±6% in the range of temperatures of interest to processing of Ni-Al powders (100– 112°C), reaching a minimum at a nominal temperature of around $T_i = 108$°C. It should be noted that coefficient K also varies within ±4% during the isothermal process, because of opposing effects of the warped ellipsoid geometry flattening, versus strain hardening and volumetric expansion of the powder materials.

During the thermal transient of Figs. 3 and 5, the dynamics of time-variable model parameters can also be derived in principle from the analytical equations. However, uncertainty in temperature dependencies of the convection coefficients h_v, h_l and surface emissivity ϵ in Eq. (4) render off-line integration of Eq. (7) impractical. Instead, real-time identification of the necessary dynamic model parameters based on their observation by the in-process BM thermostructural computational model below is employed in the context of the thermal adaptation system in what follows.

3.3. BM structure control

Open-loop control of fractal dimension output f at constant input power P could, in principle, be effected by determining off-line the integration time t of Eq. (12) to reach a target setpoint f_d, as the BM duration to be implemented in-process. However, such an approach would suffer from the uncertainty and time-variation of parameters η/K, as illustrated in the previous section, along with process disturbances, including periodic interruptions of BM to remove minor samples of the product for off-line microscopic analysis of the output f.

Instead, to regulate the fractal dimension f (from the lumped model of Eq. (12) or from the full thermostructural model in [9]) to a reference value f_d, a non-linear discrete-time deadbeat controller with power saturation is proposed. For deadbeat control, $\dot{f} = (3-f)H/K$ should approach $(f_d - f)/t_s$. Thus, by accounting for non-ideal thermal efficiency η, from Eq. (15)

$$\tilde{H}(z) = \eta\tilde{P}(z) = \frac{K}{t_s}\frac{\tilde{E}(z)}{3-\tilde{f}(z)} \tag{16a}$$

with error $\tilde{E} = \tilde{f}_d - \tilde{f}$. Power saturation is implemented by enforcing, following Ref. [15],

$$P^*(j) = \min\left[P_{\max}, \max\left\{\frac{K}{\eta t_s}\frac{E^*(j)}{3-f^*(j)}, 0\right\}\right]. \tag{16b}$$

This one-step-ahead control law attempts to provide enough input power P in order to bring the structural output f to its desired setpoint f_d in just one sampling period t_s. This saturates the input to its allowed limit $P_{\max}$ during most of BM fabrication, thus resulting in fastest and most efficient operation of the device under steady conditions, and shuts off to $P = 0$ after a short transient when f reaches f_d.

Fig. 10 exemplifies the implementation and behavior of this control scheme as determined by computer simulation, for two different

Table 2
Experimental and model variation of averaged thermostructural BM gain K at internal vial temperatures T_i in processing of Ni-Al powders.

Temperature T_i (°C)	BM Gain K (MJ) Experimental value	BM Gain K (MJ) Model estimate	Error (%)
100.2	12.17	11.85	−5.59
103.2	11.75	11.09	−5.62
108.1	9.75	9.82	+0.72
112.0	8.32	8.81	+5.89

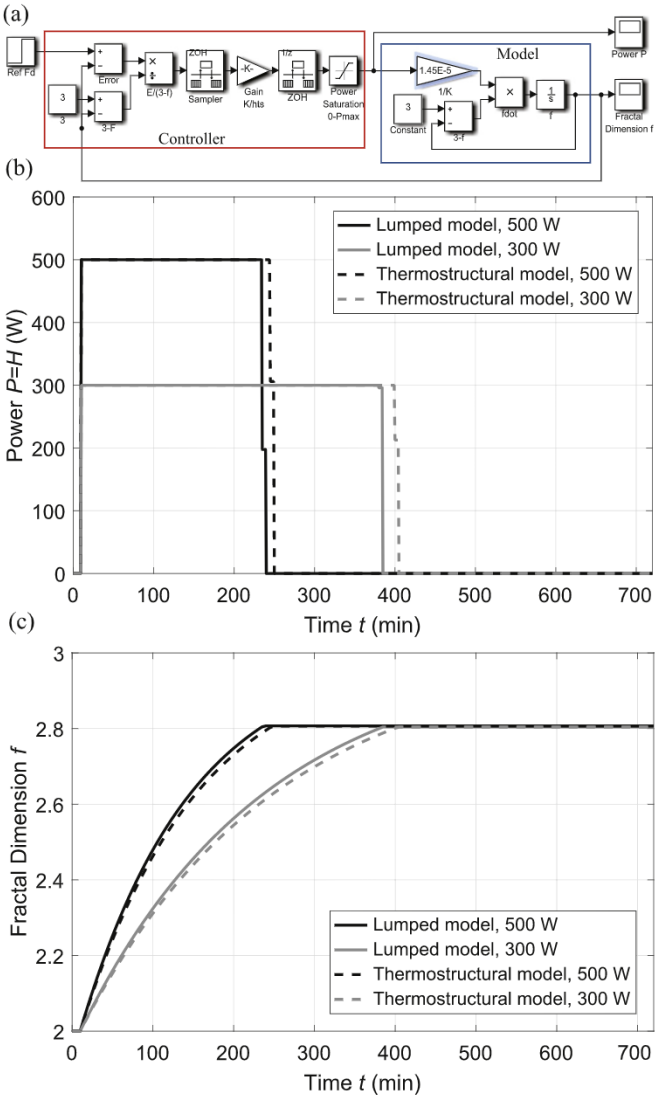

Fig. 10. Feedback control of fractal dimension output f simulated by dynamics description and structure model. (a): Implementation. (b): Input power $P = H$ responses at two saturation levels. (c): Fractal dimension f responses.

power saturation levels, at $P_{max} = 500$ W and 300W. Here, the fractal dimension f in the lumped model of Eq. (12) is regulated to a reference value $f_d = 2.8$ by the discrete controller in Eq. (16a). In the simulation, the thermostructural gain is set to $K = 69.44$kJ (fitted to the experimental data of Fig. 9 from Ref. [9], black squares); the thermal efficiency is set to $\eta = 1$; the sampling period is $t_s = 5$ min.

Fig. 10b shows the dynamic responses of power $P = H$, maintaining the constant P_{max} value as expected for about 4 and 6.5 h of processing, respectively for the two power levels, and then shutting off after a brief transient. Fig. 10c illustrates that these power schedules indeed bring the fractal dimension f to the desired value of f_d before termination of the process. Fig. 10 b and c also shows the power and fractal dimension responses when the lumped model in Eq. (12) ("Model" block on the right of Fig. 10) is replaced by the full thermostructural model described in Section 3.2 in the feedback system under the same controller ("Controller" block on the left of Fig. 10). Similar behavior is observed, with the process lasting approximately 10 min longer, presumably because of a higher value of temperature-dependent thermostructural gain K [18,19]. This is because the thermostructural model predicts slightly lower temperatures T_i than the lumped model, which result into higher plastic yield stresses of the processed materials, hence less deformation, thus slowing down the growth of fractal dimension.

4. Experimental control and adaptation

4.1. Laboratory setup and calibration

The lumped model developed in the previous sections along with the full thermostructural model [9] are calibrated against measurements on a laboratory BM device. This is a low-energy planetary BM system (Fritsch Pulverisette) in nitrogen gas (N_2) inert atmosphere, with $N_b = 5$ balls of $r_b = 5$mm radius in a rounded cylindrical 80 ml-volume vial rotating at ω up to 400 rpm and made of stainless steel. Monometallic Ni and Al powders (Alfa Aesar) are used for the experiments, with a mesh size of −325 (40 ± 4μm), a molar ratio of 1:3 (corresponding to the $AlNi_3$ intermetallic compound), and total weight of $m_{Ni} + m_{Al}$ of 32 g. Their material properties are shown in Table 3. The friction coefficient was previously calibrated to $\mu = 0.39$, see Ref. [12].

The BM setting is modified for in-process measurement of external temperature T_o on the vial cylindrical walls, with a non-rotating infrared (IR) thermocouple (Omega) fixed inside the device enclosure at a distance of 15 mm from the external perimeter of motion, see Fig. 2. Because of the planetary vial trajectory, the IR sensor is in hot-wall proximity and exposed to T_o only partially in time, indicating a lower apparent temperature T_o'. To compensate, the required sensor gain T_o/T_o' was calibrated by comparative measurements on empty vials heated uniformly at boiling water temperature (100°C), when stationary and in motion ($\omega = 300$ rpm). It was found that T_o/T_o' is independent of the rotation rate ω. The internal temperature T_i is measured off-line at the end of the experiments by quenching the BM contents (balls and particulates) into a bombshell calorimeter containing 200 ml of water at room temperature. The steady-state temperature measurements T_i and T_o are thus used to calibrate the unknown effective convection coefficient h in Eq. (4) and the useful thermal efficiency η as:

$$\eta P = H = \frac{T_i - T_o}{R} = hA(T_o - T_a) \Rightarrow \quad h = \frac{1}{RA}\frac{T_i - T_o}{T_o - T_a}, \quad \eta = \frac{T_i - T_o}{PR}. \tag{17}$$

In addition, the steady-state heat input H above is used to calibrate the thermostructural gain K of the lumped model in Eq. (12), as well as the heat source efficiency factor of the full thermostructural model [14], by matching the predicted fractal dimension f responses to off-line measurements on laboratory micrographs. For example, Fig. 11 compares the BM particulate structures, obtained via scanning electron microscopy (SEM) [23], to the predictions of the full thermostructural model, along with their fractal dimension values after 2, 6 and 10 h of BM, regulated to $\omega = 300$ rpm. The micrographs show a progressive structural refinement from a globular agglomerate to a lamellar network microstructure of gradually increasing fractal dimension, with the calibrated model predictions matching the experimental results within a ±3% error on f. In comparison to the simulated responses of Fig. 10, however, lower values of f over time t towards steady state (or, equivalently, longer times t required to obtain a desired value of f) result from the calibrated value of thermal efficiency reduced to $\eta = 0.73$, therefore yielding lower than previously assumed ideal ($\eta = 1$) heat dissipation $H = \eta P$.

Table 3
Ball-milled and impactor material properties (room temperature).

Material/Properties	Aluminum (99.5%)	Nickel (99.95%)	Steel (1.4404)
Thermal conductivity k (W/m K)	205	91	15.5
Specific heat capacity c (J/kg K)	897	444	510
Density ρ (kg/m^3)	2702	8908	7955
Yield Tensile Stress σ_y (MPa)	17.5	140	290
Yield Elastic Strain ε_y [10^{-3}]	0.25	0.823	1.47

4.2. Adaptive control system

The objective of this paper is to enable in-process control of the BM particulate structure on the laboratory system to a reference value of fractal dimension f_d which optimizes reactivity performance. Such control is hindered by the unavailability of real-time, non-destructive, non-invasive imaging data during the BM process. In lieu of experimental measurements f, the estimated fractal dimension $\hat{f}$, as determined by real-time execution of the model in Ref. [9], can be used for feedback as in the previous section. Specifically, the model is run in parallel to the laboratory setting as a thermostructural process observer, under equivalent modulation of input power P.

To reconcile dynamic discrepancies between the hardware setup and the software model during BM fabrication, adaptation is needed in the control scheme. The strategy adopted in this work is based on real-time comparison of the IR measurements of external temperature T_o to the model predictions of $\hat{T}_o$, achieved via a thermal model equivalent to Eq. (6). The resulting thermal estimate error $e = \hat{T}_o - T_o$ is thus used for model reference adaptive control (MRAC) [15], as illustrated in Fig. 12. This scheme uses the accumulated estimation error e as a measure of thermal deficit of the actual process with respect to its model. The error is thus compensated by adding a supplementary term P' to the input of the BM device only. Therefore, this approach compensates for the temperature deficiency by further escalating the process [15]:

$$P'^*(j) = K' \sum_{i=0}^{j} e^*(i) \Rightarrow \frac{\tilde{P}'(z)}{\tilde{e}(z)} = \frac{K'z}{z-1} = G'(z) \tag{18}$$

with $\tilde{e} = \tilde{\hat{T}}_o - \tilde{T}_o$, where K' is an adaptation gain. This is equivalent to a linear model follower scheme [15], so named because for a linear process $G(z)$ and model $\hat{G}(z)$ driven by a linear controller $G_c(z)$, the closed-loop behavior for increasing K' can be shown to approach a linear pulse transfer function $G_{CL}(z)$ such that [15]

$$G_{CL}(z) \to \frac{G_c(z)\hat{G}(z)}{1 + G_c(z)\hat{G}(z)} \tag{19}$$

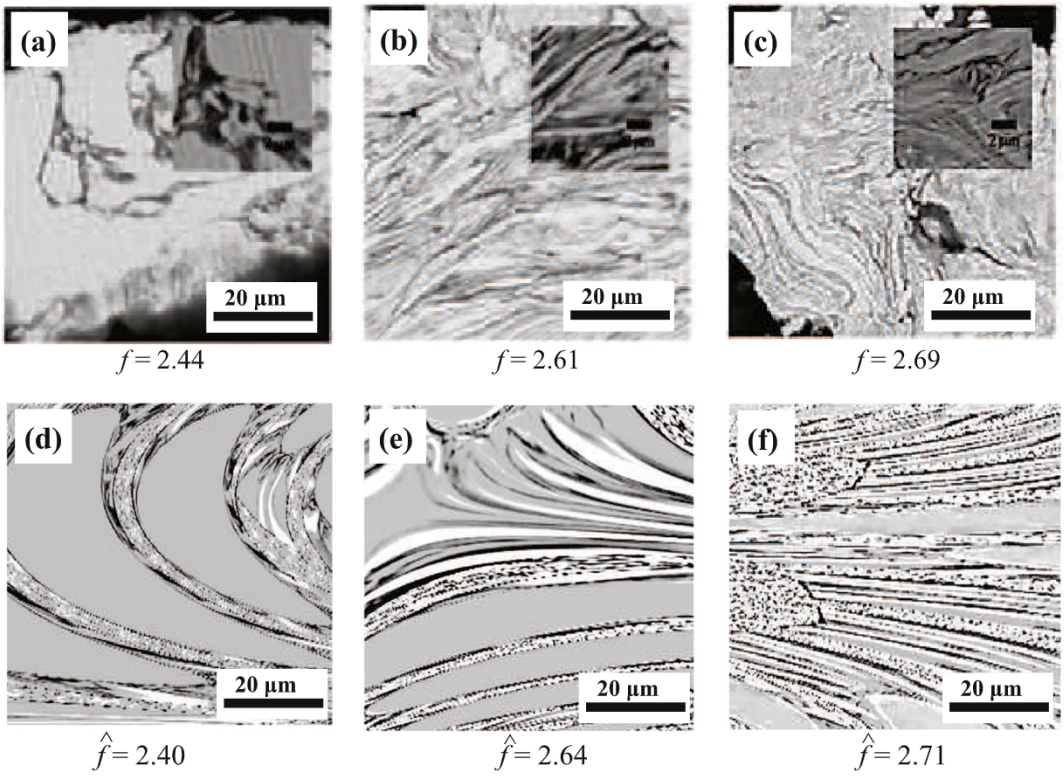

Fig. 11. Microstructures and fractal dimensions of particulates during BM; SEM micrographs and f: (a) 2 h, (b) 6 h, (c) 10 h [23]; Model simulations and $\hat{f}$: (d) 2 h, (e) 6 h, (f) 10 h.

as $K' \to \infty$. It is noteworthy that in the closed loop G_{CL} of Eq. (18), the process G has been effectively replaced by its model $\hat{G}$. This illustrates that, with the augmented input, this MRAC system essentially forces the process to adapt and behave like its model, according to some pre-designed and optimized closed-loop reference behavior for the model, determined via simulation.

4.3. Experimental testing

In a laboratory testing, the temperature T_o from the IR thermocouple data logger is fed back to the control computer, which modulates the power P through the rotation rate ω setpoint in the BM device controller. The same computer is used to run the

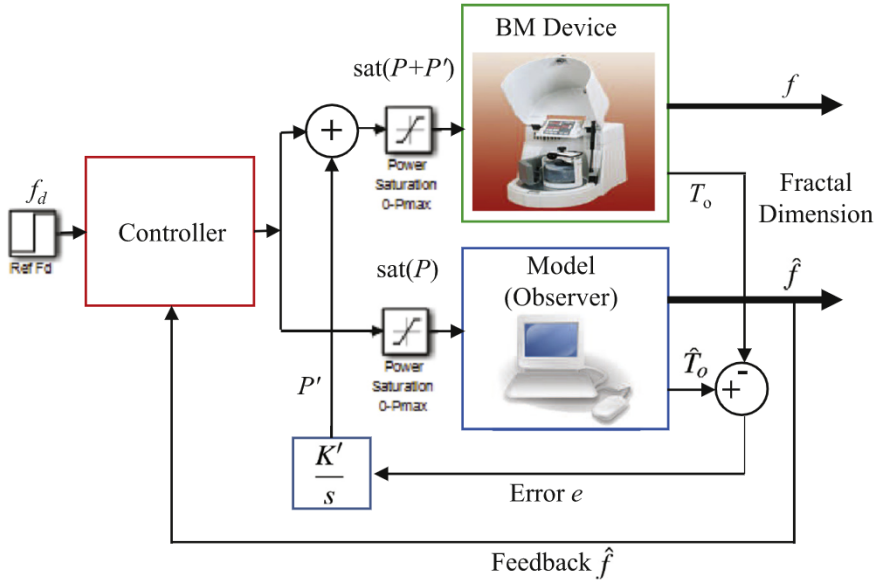

Fig. 12. Implementation of model reference adaptive control with the thermostructural model (TM) or the lumped model (LM) as process observers during laboratory device testing.

thermostructural model as a real-time observer of the particulate microstructure and its fractal dimension $\hat{f}$, along with temperature estimate $\hat{T}_o$. The control law of Eq. (16a) with power saturation at $P_{\max} = 300$ W is implemented with sampling period $t_s = 5$ min. The adaptation law of Eq. (18) for P' is run with gain $K' = 4.5$ W/K. The desired reference value for the fractal dimension f is set to $f_d = 2.65$. The implementation of this control scheme is presented in Fig. 12.

Fig. 13a shows the saturated response for the power input to the observer sat(P) (solid lines) and the power input to the device sat $(P+P')$ (dashed lines). Fig. 13b shows the response of measured (solid lines) and estimated (dashed lines) external temperatures T_o and $\hat{T}_o$, respectively. Finally, Fig. 13c displays the time history of fractal dimension $\hat{f}$ (lines), together with actual values of f measured (markers) on micrographs from stopped tests. In these figures, the label "TM" indicates that the observer is the full thermostructural model, while the label "LM" indicates that the observer is the lumped model.

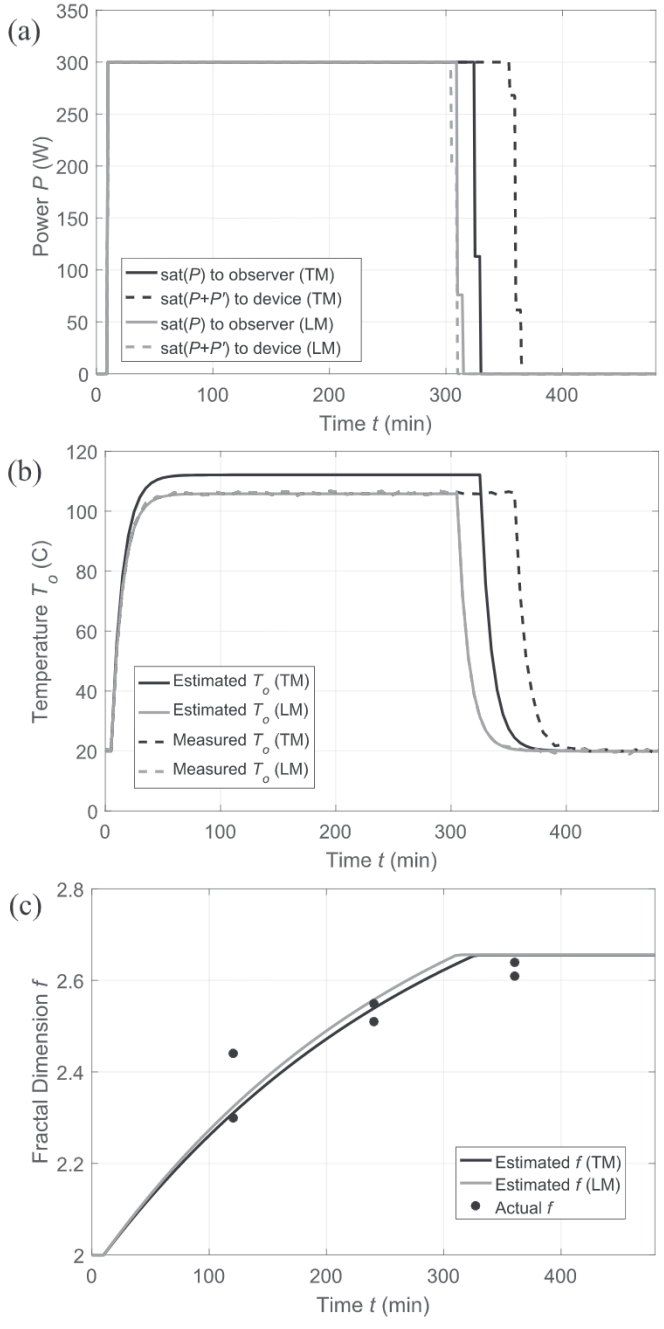

Fig. 13. Performance of model reference adaptive control with the thermostructural model (TM) or the lumped model (LM) as process observers during laboratory device testing. (a): Input power P responses. (b): Temperature T_o (measured and estimated) responses. (c): Output fractal dimension f responses.

When the full thermostructural model is used as observer, Fig. 13a demonstrates that the input saturation ceiling $P_{\max}$ prevents the extra adaptation term P' to be provided to the device during the steady state of the process. As a consequence, the actual T_o remains below the estimated $\hat{T}_o$, see Fig. 13b. Therefore, the error $e = \hat{T}_o - T_o$ remains steady during most of the response and contributes to an increasing value of P', according to Eq. (18). When the feedback estimate $\hat{f}$ approaches f_d, see Fig. 13c, and the controller shuts off the input to the observer at around $t = 5.5$ h, the accumulated P' continues to provide actual input to the BM device, which remains in operation for another ~0.5 h. During this additional time, the estimated temperature $\hat{T}_o$ drops below the actual temperature T_o. This causes the error e to become negative, gradually draining P' until its depletion, when the device is also stopped. Therefore, the BM setup adaptation to its reference model observer is implemented by prolonging the process rather than intensifying it. This compensates for the deficiency in thermal exposure of the BM materials, and eventually allows the achievement of the desired particulate structure, see Fig. 13c.

It is interesting to discuss the case where the lumped model of Eqs. (6) and (12) is used as the reference model-observer in Fig. 12, while the controller and BM device remain as before. It can be seen that the temperature estimates $\hat{T}_o$ slightly underestimate the measured temperatures T_o. This results in small negative errors e and adaptation P', shutting off the device 5 min before the reference model, see Fig. 13a. In this shorter period, the lumped model in Eq. (12) over-predicts the estimated fractal dimension $\hat{f}$, with the resulting actual f falling below the desired f_d value, see Fig. 13c. It can be concluded that an ad-hoc calibration of the thermostructural gain K to the temperature levels of each BM run would be necessary for the simpler lumped model to match the microstructure prediction accuracy of the more comprehensive, but computationally intensive, full thermostructural model of the BM particulate.

5. Conclusion and future work

This work investigated thermal and structural modeling and regulation of the ball milling process, directly addressing its challenges of inaccessibility to real-time, non-destructive, non-invasive imaging measurements in the enclosed rotating vial during the process. An adaptive control system for the BM particulate microstructure was introduced and tested in the laboratory, using proxy feedback of fractal dimension on micrographs from a real-time computational model serving as an observer and model reference. Adaptation was achieved by comparison of the temperature predictions of the model to infrared thermal measurements obtained on the rotating vial external surface during the process. The control scheme was designed on the basis of a lumped model of the heat transfer dynamics of the process, as well as via a formulation of the fractal structure dynamics. This regulation system achieves the desired refinement in the BM particulate microstructure by controlling the process duration as to insure the necessary thermal exposure of the BM products. As such, this research adds an essential step in the literature efforts for thermostructural control of ball milling [24-29].

While such regulation of the fractal geometry in the internal microstructure of BM particulates is a necessary condition to achieve the desired thermal reactive performance upon ignition, control of the material aspects in this structure is also needed. Specifically,

the bimetallic interfaces in the material (Figs. 1 and 11) upon exposure to elevated temperatures give rise to mutual elemental diffusion yielding the respective composition fields near the boundaries. These reduce the available Gibbs free energy and chemical reaction potentials, thus affecting the product quality for a certain fractal geometry. In poorly controlled BM processing, especially at higher temperatures and duration, the resulting solid solutions may produce intermetallics (nickel aluminides) during fabrication, therefore annihilating the respective exothermic enthalpies. Dynamic modeling of diffusion for in-process control of composition is another crucial aspect of BM regulation, which has been recently investigated in Ref. [30]. However, simultaneous multivariable control of fractal dimension and diffusion has not been reported in the literature and is subject of future research.

Acknowledgments

This research was supported in part by a Khalifa University Internal Research Fund (Level 1) award. The raw/processed data required to reproduce these findings cannot be shared at this time as the data also forms part of an ongoing study.

References

[1] D. Adams, Reactive multilayers fabricated by vapor deposition: a critical review, Thin Solid Films 576 (2015) 98–128.
[2] J. Wang, E. Besnoin, A. Duckham, S. Spey, M. Reiss, O. Knio, M. Powers, M. Whitener, T. Weihs, Room-temperature soldering with nanostructured foils, Appl. Phys. Lett. 83 (19) (2003) 3987–3989.
[3] I.E. Gunduz, K. Fadenberger, M. Kokonou, C. Rebholz, C.C. Doumanidis, Investigations on the self propagating reactions of nickel and aluminum multilayered foils, Appl. Phys. Lett. 93 (13) (2008) 4101.
[4] A. Hadjiafxenti, I.E. Gunduz, C. Tsotsos, T. Kyratsi, C.C. Doumanidis, C. Rebholz, Synthesis of reactive Al/Ni structures by ball milling, Intermetallics 18 (11) (2010) 2219–2223.
[5] C. Rebholz, I.E. Gunduz, T. Ando, C.C. Doumanidis, Miniature thermal matches: from nanoheaters to reactive fractals, Mater. Res. Express 2 (4) (2015) 045009.
[6] B. Mandelbrot, The Fractal Geometry of Nature, W.H. Freeman & Co.. 1983.
[7] S. Talu, Micro and Nanoscale Characterization of Three Dimensional Surfaces, Basics and Applications, Napoca Star Publishing House, Cluj-Napoca, Romania, 2015.
[8] A. Rogachev, N. Shkodich, S. Vadchenko, F. Baras, D.Y. Kovalev, S. Rouvimov, A. Nepapushev, A. Mukasyan, Influence of the high energy ball milling on structure and reactivity of the Ni + Al powder mixture, J. Alloys Compd. 577 (2013) 600–605.
[9] C.C. Doumanidis, I. Gunduz, C. Rebholz, C.C. Doumanidis, Real-time computational model of ball-milled fractal structures, J. Nanotechnol. Eng. Med. 6 (3) (2015) 031001.
[10] A. Pomerleau, D. Hodouin, A. Desbiens, É. Gagnon, A survey of grinding circuit control methods: from decentralized PID controllers to multivariable predictive controllers, Powder Technol. 108 (2) (2000) 103–115.
[11] X.S. Chen, Q. Li, S.M. Fei, Constrained model predictive control in ball mill grinding process, Powder Technol. 186 (1) (2008) 31–39.
[12] C.C. Doumanidis, H.A. Al Kaabi, A.S. Alzaabi, I.E. Gunduz, C. Rebholz, C.C. Doumanidis, Brownian-like kinematics of ball milling for particulate structural modeling, Powder Technol. 301 (2016) 1077–1084.
[13] H.S. Carslaw, J.C. Jaeger, Conduction of Heat in Solids, 2nd ed. ed., Oxford University Press, New York, NY, 1959.
[14] M. Aureli, C.C. Doumanidis, I.E. Gunduz, A.G.S. Hussien, Y. Liao, S. Jaffar, C. Rebholz, C.C. Doumanidis, Non-equilibrium microscale thermomechanical modeling of bimetallic particulate fractal structures during ball milling fabrication, J. Appl. Phys. 122 (2017) 025118.
[15] K.J. Åström, B. Wittenmark, Adaptive Control, Addison-Wesley. 1995.
[16] L. Takacs, J.S. McHenry, Temperature of the milling balls in shaker and planetary mills, J. Mater. Sci. 41 (16) (2006) 5246–5249.
[17] S.Q. Xi, J.G. Zhou, X.T. Wang, Research on temperature rise of powder during high energy ball milling, Powder Metall. 50 (4) (2007) 367–373.
[18] S.J. Rosenberg, Nickel and Its Alloys, Tech. Rep., vol. 106, Institute for Materials Research, National Bureau of Standards, Washington, D.C, 1968,
[19] Y.S. Touloukian, C.Y. Ho, Properties of Aluminum and Aluminum Alloys, Tech. Rep., vol. 21, Thermophysical Properties Research Center, Purdue University, W. Lafayette, IN, 1973,
[20] M. Aureli, C.C. Doumanidis, I.E. Gunduz, A.G.S. Hussien, Y. Liao, C. Rebholz, C.C. Doumanidis, Mechanics and energetics modeling of ball-milled metal foil and particle structures, Acta Mater. 123 (2017) 305–316.
[21] D. Terzopoulos, D. Metaxas, Dynamic 3D models with local and global deformations: deformable superquadrics, IEEE Trans. Pattern Anal. Mach. Intell. 13 (1991) 703–714.
[22] A.F. Bower, Applied Mechanics of Solids, CRC Press. 2009.
[23] Z. Gu, Q. Cui, J. Chen, J. Buckley, T. Ando, D. Erdeniz, P. Wong, A. Hadjiafxenti, P. Epaminonda, I.E. Gunduz, C. Rebholz, C.C. Doumanidis, Fabrication, characterization and applications of novel nanoheater structures, Surf. Coat. Technol. 215 (2013) 493–502.
[24] T. Kopetzky, G. Hefter, R. Wieser, T. Walther, G. Schubert, How to make milling more energy efficient, Process Worldw. 13 (2011) 19–22.
[25] S.J. McGarel, Model predictive control for SAG milling in minerals processing, Tech. Rep. RSWP11-AP002A-EN-P, Rockwell Automation. 2011,
[26] J. Xu, R. Zhang, J. Wang, S. Ge, H. Zhou, Y. Liu, P. Chen, Effective control of the microstructure of carbide-derived carbon by ball-milling the carbide precursor, Carbon 52 (2013) 499–508.
[27] K. Morsi, S. Shinde, E.A. Olevsky, Self-propagating high-temperature synthesis (SHS) of rotator mixed and mechanically alloyed Ni/Al powder compacts, J. Mater. Sci. 41 (17) (2006) 5699–5703.
[28] R.K. Gupta, D. Fabijanic, T. Dorin, Y. Qiu, J.T. Wang, N. Birbilis, Simultaneous improvement in the strength and corrosion resistance of Al via high-energy ball milling and Cr alloying, Mater. Des. 84 (2015) 270–276.
[29] M. Raviathul Basariya, V.C. Srivastava, N.K. Mukhopadhyay, Microstructural characteristics and mechanical properties of carbon nanotube reinforced aluminum alloy composites produced by ball milling, Mater. Des. 64 (2014) 542–549.
[30] M. Aureli, C.C. Doumanidis, I.E. Gunduz, A.G.S. Hussien, Y. Liao, N. Kostoglou, C. Rebholz, C.C. Doumanidis, Bimetallic diffusion modeling and temperature regulation during ball milling, Mater. Des. 155 (2018) 233–243.